

Direct Observation of Charge-Carrier Heating at WZ–ZB InP Nanowire Heterojunctions

Chaw Keong Yong,[†] Jennifer Wong-Leung,[‡] Hannah J. Joyce,[†] James Lloyd-Hughes,[†] Qiang Gao,[‡] H. Hoe Tan,[‡] Chennupati Jagadish,[‡] Michael B. Johnston,[†] and Laura M. Herz^{*,†}

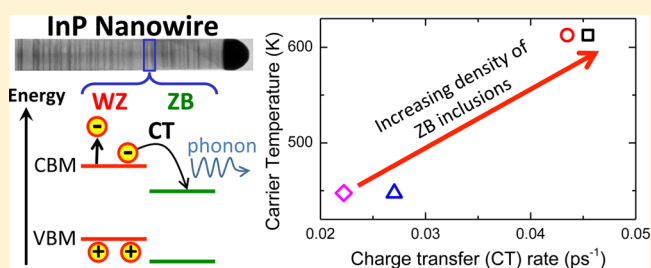
[†]Department of Physics, University of Oxford, Clarendon Laboratory, Parks Road, Oxford OX1 3PU, U.K.

[‡]Department of Electronic Materials Engineering, Research School of Physical Sciences and Engineering, Institute of Advanced Studies, Australian National University, Canberra ACT 0200, Australia

S Supporting Information

ABSTRACT: We have investigated the dynamics of hot charge carriers in InP nanowire ensembles containing a range of densities of zinc-blende inclusions along the otherwise wurtzite nanowires. From time-dependent photoluminescence spectra, we extract the temperature of the charge carriers as a function of time after nonresonant excitation. We find that charge-carrier temperature initially decreases rapidly with time in accordance with efficient heat transfer to lattice vibrations. However, cooling rates are subsequently slowed and are significantly lower for nanowires containing a higher density of stacking faults. We conclude that the transfer of charges across the type II interface is followed by release of additional energy to the lattice, which raises the phonon bath temperature above equilibrium and impedes the carrier cooling occurring through interaction with such phonons. These results demonstrate that type II heterointerfaces in semiconductor nanowires can sustain a hot charge-carrier distribution over an extended time period. In photovoltaic applications, such heterointerfaces may hence both reduce recombination rates and limit energy losses by allowing hot-carrier harvesting.

KEYWORDS: Nanowires, hot carriers, type II heterojunctions, stacking faults, photovoltaics



The successful incorporation of III–V semiconductor nanowires (NWs) into optoelectronic and photovoltaic devices as both elements and interconnects has sparked intense interest in the nature of charge carrier dynamics in such nanostructured materials.^{1–3} In particular, InP NWs are promising for applications ranging from high-speed optoelectronic devices⁴ to photovoltaic cells,^{5,6} and sensitive photodetectors.³ It has been shown that the crystal structure of InP NWs can be formed preferentially in either the zinc-blende (ZB)^{7,8} or wurtzite (WZ) phase,^{9,10} depending on the growth conditions. Moreover, the existence of a polytypic phase due to stacking faults along the growth axis of nanowires has been demonstrated recently to have significant implication for the band alignment and electronic transitions.^{11–14} Both theoretical¹⁵ and experimental results^{14,16} have demonstrated that the band gap energy of InP differs by ≈ 80 meV between the WZ and ZB crystal structures and that staggered type II band alignment is formed at their interface, with the conduction band minimum and the valence band maximum in ZB respectively located ≈ 129 and ≈ 45 meV below those in WZ. Recent optical studies further show that for nanowires with predominant WZ crystal structure a short ZB layer sandwiched between two WZ segments can form a quantum well (QW), for which the subband energy depends on the thickness of the ZB segments.^{11,13,14,16} The spatial separation of holes in the WZ phase and electrons in the QWs further reduces the

photoluminescence (PL) recombination rate observed in the nanowires because of restrictions imposed by momentum and energy conservation in semiconductors.^{13–15}

Carrier cooling in semiconductors has been extensively studied both in the bulk and in nanostructures.^{17–21} A thorough investigation of the dynamics of carrier cooling is known to be crucial for the design of various optoelectronic devices. For example, carrier cooling controls and competes with other processes such as multiexciton generation and hot-carrier extraction in hybrid organic photovoltaics and hence affects device efficiencies.^{21–23} It has been shown that, following nonresonant excitation, hot-carrier cooling is initially dominated by the emission of longitudinal optical phonons. As the carrier temperature approaches the lattice temperature, subsequent energy relaxation occurs more slowly through interactions with acoustic phonons. At high injection density situations, the filling of nonequilibrium acoustic phonon states can further reduce the carrier cooling rate, a phenomenon referred to as the “acoustic phonon bottleneck”.^{18,24,25} Similarly, the occurrence of charge transfer at type II semiconductor heterojunctions ought to be associated with a

Received: June 5, 2013

Revised: July 30, 2013

Published: August 6, 2013



transfer of excess energy to the lattice and the electronic system. However, no systematic study has so far been performed to investigate how such additional energy release affects the intraband energy-loss rate of hot carriers in semiconducting nanowires.

In this Letter, we provide direct evidence that the presence of type II heterojunctions reduces the charge-carrier cooling rate in semiconductor nanowires. We investigated the charge-carrier dynamics in InP nanowire ensembles containing a range of densities of stacking faults that result in staggered (type II) band offsets along the growth axis of the nanowires. Analysis of PL emission maps shows that the presence of WZ–ZB type II interfaces in InP nanowires can be deduced from the occurrence of broader spectral features that increasingly shift toward WZ emission as the excitation fluence is increased. We demonstrate that an increasing density of such interfaces in a nanowire will induce faster PL emission quenching, which is hence dominated by the rate of charge transfer across interfaces. We find that such dynamics of charge transfer across WZ–ZB interfaces exhibit strong correlation with the time-dependent rates with which intraband charge carrier cooling occurs. Following nonresonant excitation, the temperature of charge carriers, as extracted from the high-energy tail of the time-dependent PL spectra, is found to decrease with time in accordance with rapid charge carrier cooling. However, the cooling rates are significantly lower for nanowires containing a higher density of stacking faults. We conclude that the transfer of charges across the type II interface releases additional energy to the lattice, which raises the phonon bath temperature above equilibrium and impedes the carrier cooling occurring through interaction with longitudinal optical phonons. These results demonstrate that type II heterointerfaces in semiconductor nanowires can allow for a hot charge-carrier distribution to be maintained over an extended time period. Such excess energy can potentially be harvested when these nanowires are embedded in an organic matrix, thus lowering the energy threshold requirements for charge transfer in hybrid photovoltaic materials.

The InP nanowires used in this study were fabricated on poly(L-lysine)-treated InP (111)B substrates using a metal-organic chemical vapor deposition (MOCVD) technique. Four sets of nanowires were fabricated whose diameters were controlled by the size of the colloidal Au nanoparticles (20, 30, 50, or 80 nm) acting as catalyst. The nanowires were grown at a pressure of 100 mbar and a total gas flow rate of 15 SLM. Growth was performed at 420 °C for 20 min using trimethylindium and phosphine precursors with a V/III ratio of 700. Field emission scanning electron microscopy (FESEM) was carried out using a Hitachi S4300 FESEM at an accelerating voltage of 5 kV. For transmission electron microscopy (TEM) investigations, nanowires were first mechanically transferred to holey carbon grids. TEM was performed using a Phillips CM300 TEM operated at 300 kV. At least five nanowires were examined from each sample. Nanowires were examined for crystal structure and stacking faults over their entire length. Figure 1a shows a representative SEM image of nanowires and Figure 1b a high-resolution TEM image. While the crystal structure of the nanowires is predominantly WZ, a considerably high volume fraction of ZB can be clearly identified from the TEM image. This suggests the presence of a high density of stacking faults in the nanowires.^{11,13,14} We find that the ZB sections vary in thickness up to several bilayers, and they are unevenly distributed along

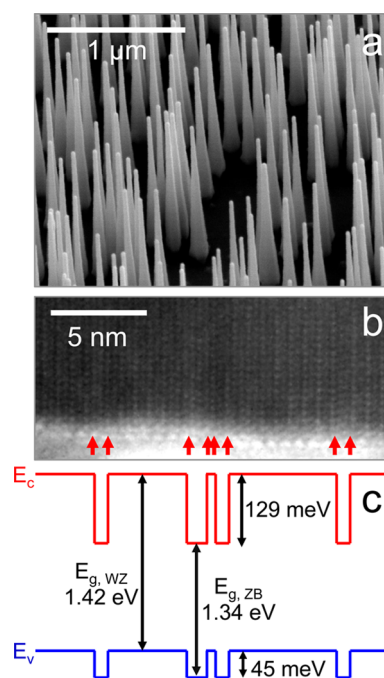


Figure 1. (a) Scanning electron microscopy image of InP nanowires of 50 nm average diameter, as-grown on InP substrates at a tilt of 40°. Scale bar is 1 μm . (b) High-resolution transmission electron microscopy image of a typical InP nanowire from the 50 nm diameter ensemble, featuring predominantly WZ structure with stacking faults. Arrows indicate the stacking sequences, i.e., polytypic transitions between WZ and ZB. (c) The approximate corresponding band diagram at room temperature. The band diagram was constructed from published experimental and theoretical data for band gaps and band offsets.^{14–16}

the growth axis of the nanowires. Furthermore, the nanowires exhibit sizable tapering, as seen in the SEM image. We therefore estimate the cross section of the nanowires from the SEM by averaging over the length of nanowires. We find that the nanowires exhibit very similar standard deviation of their diameter distribution (see Supporting Information). The average diameters of the nanowire ensembles were $\langle d \rangle$ of 50, 85, 135, and 160 nm for nanowires growth seeded by Au colloids with diameter of 20, 30, 50, and 80 nm, respectively. Hereafter, we refer to, for example, the nanowire ensemble with $\langle d \rangle$ of 50 nm as 50 nm-NWs. To eliminate the otherwise dominant photoluminescence and photoconductivity signals that would originate from the InP substrate, nanowires were subsequently transferred onto z-cut quartz substrates by gently rubbing the two substrate together resulting in nanowires that lie flat on the quartz substrate.

Figure 1c illustrates the band diagram to be expected along the axis of a sample nanowire, given the known band gaps and offsets for InP with ZB and WZ structure. The type II band alignment across the WZ–ZB heterojunctions results in favorable formation of spatially localized photoexcited electrons in the ZB and holes in the WZ segments.^{13–16,26} Here, WZ–ZB–WZ sequences can define quantum wells (QWs) for electrons with the confinement energy varying with the thickness of the ZB segment.^{11,13,14,16} Low-temperature PL measurements have revealed that the emission arising from the spatially separated electron–hole pairs is energetically below the WZ gap and long-lived as a result of restrictions imposed by

momentum and energy conservation in bulk semiconductors.^{13–15}

To examine the emission arising from such spatially separated electron–hole pairs in the InP nanowires, we conducted time-integrated PL (TIPL) emission measurements at a substrate temperature of 77 K. Figure 2a,b displays the

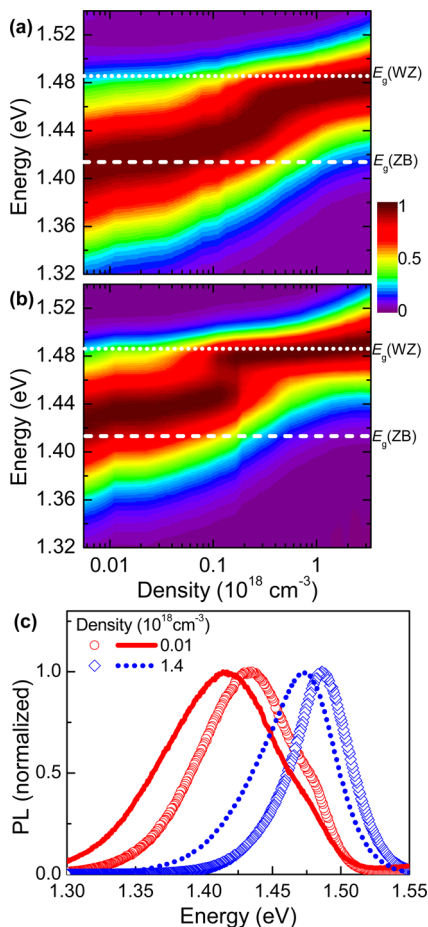


Figure 2. TIPL spectra maps taken at 77 K for (a) 50 nm-InP NWs and (b) 160 nm-InP NWs showing the intensity (on a linear false color scale) as a function of initial charge injection density (horizontal scale) and emission energy (vertical scale). For clarity, all spectra were normalized to their maximum intensity. The dotted and dashed lines indicate the bandgap energy of the WZ phase $E_g(\text{WZ})$ and the ZB phase $E_g(\text{ZB})$ at 77 K, respectively. (c) Individual TIPL spectra for 50 nm-InP NWs (dashed and dotted lines) and 160 nm-InP NWs (circles and diamonds), displaying the evolution of the PL spectra as the initially injected charge carrier density is increased from 1×10^{16} to $1.4 \times 10^{18} \text{ cm}^{-3}$. Corresponding data for 85 nm-InP NWs and 135 nm-InP NWs are shown in the Supporting Information.

false-color image spectral maps for 50 nm-InP NWs and 160 nm-InP NWs, respectively, where the vertical and horizontal axes respectively show the emission energy and the excitation density (on a logarithmic scale). The false-color image spectral maps for nanowires with $\langle d \rangle$ of 85 and 135 nm are shown in the Supporting Information. For low excitation densities, spectra are broad and emission energies located between the WZ and ZB band edges. The broad, low-energy spectra recorded for low fluence are consistent with emission originating from spatially separated electron–hole pairs with electrons and holes located in the ZB and WZ segments of the nanowires, respectively.^{13,14} The broad spectral line width may

arise from an uneven distribution of ZB segment widths in the nanowires, which results in a distribution of quantum confined states (see Supporting Information).^{11,13,14,16} With increasing excitation density, the spectra narrow and shift to center at the WZ band edge; i.e., the emission originates predominantly from the WZ segments of the wires. Since these segments are relatively long according to TEM images (see Figure 1b), there is comparatively little spectral broadening associated with the emission from the WZ phase, and the emission spectra consequently become narrower. It should be noted that the quantum confinement induced by the diameter of these nanowires is negligible,¹⁵ and hence the tapering observed along the growth axis of the nanowires is unlikely to give any significant PL spectral broadening. There are two possible scenarios which may explain the gradual shift with increasing fluence in the preferential emission from spatially separated electron–hole pairs to that originating from just the WZ segments. First, as the density of injected charge carriers increases, superlinear bimolecular recombination²⁷ in the WZ phase will lead to enhanced photon emission rates. In contrast, the competing process of electron transfer from WZ to ZB segments is only proportional to the electron density and therefore scales linearly with excitation fluence. As a result, recombination processes in WZ will at high fluence increasingly dominate over charge-transfer processes into ZB segments, and the emission spectra will acquire the signature of the WZ phase. A second explanation for these effects could be that saturation of states available in the ZB segments results in an enhancement of WZ emission for high fluences as this may result in lowered electron transfer from WZ into ZB segments. However, we show below that this is not in fact observed in time-resolved studies, leaving the first explanation as the most likely.

Given that these NW emission spectra are clearly influenced by the presence of stacking faults, it will be useful to compare spectra recorded at similar excitation fluences for the 50 nm-NW and 160 nm-NW ensembles. Figure 2c shows individual normalized PL spectra for both nanowire sets, for two extreme charge injection densities of 1×10^{16} and $1.4 \times 10^{18} \text{ cm}^{-3}$. From these sample spectra, and the full density maps (Figure 2a,b), it is apparent that the emission line width for a given excitation fluence is broader for the 50 nm-InP NWs than for the 160 nm-InP NWs throughout all injection densities. We hence conclude that the 50 nm-InP NWs contain a higher density of stacking faults than the 160 nm-InP NWs. This finding also agrees with the fact that at the highest fluences explored the emission peak for the 50 nm-InP NWs still remains red-shifted from the band gap of WZ (Figure 2a). The two nanowire ensembles therefore not only differ in average nanowire diameters but also in the density of stacking faults present. An equivalent analysis of the spectral maps collected from 85 nm-NW and 135 nm-NW ensembles (see Supporting Information) shows that again the former supports a higher defect density than the latter. As we show below, there is a clear inverse correlation between nanowire diameter and induced stacking fault density, which may arise from the differential dynamics of growth induced by the size of the Au nanoparticles employed in this study.

To establish the influence of stacking-fault density on the charge carrier dynamics occurring at such interfaces, we use a combined set of time-resolved photoluminescence and THz conductivity probes. While photoluminescence measurements^{27,28} are sensitive to electron–hole recombination and

hence the density of both species, terahertz conductivity spectroscopy²⁹ is sensitive to charge carriers with high mobility, i.e., only the electrons in InP.³⁰ Combining the two techniques therefore enables us to separate charge transfer dynamics occurring across the type II interfaces from pure charge recombination effects. Measurements were conducted at room temperature (300 K) as it is essential to examine the ultrafast carrier dynamics as they would occur in practical nanodevices. Full details of both the transient PL up-conversion setup (PLUC) and the optical-pump terahertz-probe (OPTP) experiment are provided in refs 30 and 31 and in the Supporting Information. For PLUC, nanowires were excited nonresonantly at a photon energy of 1.68 eV and the PL emission monitored near the bandgap energy of the WZ phase (1.43 eV at room temperature) with a temporal resolution of 200 fs. For OPTP, excitation was also nonresonant (1.55 eV), and similar excitation fluence to that employed for PLUC was used. For ease of discussion, we again focus here on the two nanowire sets with extreme diameters and stacking fault densities, i.e., 50 nm-InP NWs and 160 nm-InP NWs. Matching data for 85 nm-NW and 135 nm-NW ensembles are provided in the Supporting Information, which shows analogous trends and will be included in a comparative discussion further below.

Figure 3 shows that the photoinduced conductivity of InP NWs measured using OPTP has a decay lifetime in excess of 1

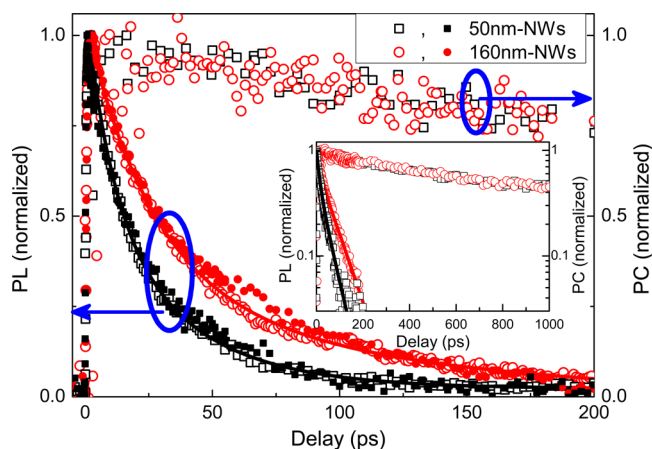


Figure 3. Transient photoluminescence (PL) and photoconductivity (PC) decays of InP NWs measured at 300 K as a function of time after excitation. For transient PL measurements, the nanowires were excited at a photon energy of 1.68 eV with pulse fluences generating an initially injected charge carrier density of $1.4 \times 10^{18} \text{ cm}^{-3}$ (empty symbols) and $0.7 \times 10^{18} \text{ cm}^{-3}$ (solid symbols). The PL emission was detected at the energy corresponding to the bandgap of the WZ phase (1.44 eV). For photoconductivity measurements, the samples were excited at a photon energy of 1.55 eV with initial charge carrier injection of $1.4 \times 10^{18} \text{ cm}^{-3}$. The inset shows the same data over an extended time range of over 1000 ps and on a logarithmic y -axis scale.

ns and exhibits negligible dependence on the average nanowire diameter. For InP nanowires, the photoconductivity is dominated by the electron density as the effective mass of electrons is significantly smaller than that of holes in InP.³² As demonstrated in a recent study, such long-lived electron lifetime is indicative of an ultralow surface recombination velocity in InP nanowires.^{30,33} In contrast, the PL emission dynamics from WZ phases observed for the same two sets of nanowires (Figure 3) exhibits rapid quenching within the 200 ps observation window. For the two photoexcitation densities

at which PLUC data was recorded, 0.7×10^{18} and $1.4 \times 10^{18} \text{ cm}^{-3}$, no differences in decay dynamics are discernible. However, clear changes in PL decay lifetime are apparent for the two ensembles with different nanowire diameters. While the time taken for the emission to decay to $1/e$ of its initial value is 42 ps for 160 nm-InP NWs, this decreases further to 21 ps for the 50 nm-InP NWs sample. We can rule out the possibility of significant Auger recombination occurring in our nanowires under the injection densities used here. This is because such processes are rather slow and inefficient in bulk semiconductors due to energy and momentum conservation requirements.^{20,34} Even in quantum dots, where such restrictions are lifted, noticeable Auger recombination only occurs at charge densities that are over an order of magnitude higher than those employed here.^{20,35} Since the PL intensity is proportional to the product of the electron and hole density distribution at the same k space, and since OPTP measurements indicate that the electron density appears fairly constant over the first hundred picoseconds, we conclude that the rapid PL decay is attributable to the rate of spatial electron–hole pair separation. Here, the presence of an energetic offset across the WZ–ZB type II heterojunction provides efficient channels for electron injection from the conduction band of WZ into the energetically lower-lying electronic states of ZB in the nanowires. These findings are in agreement with our earlier discussion of the time-integrated PL spectra which revealed that the 50 nm-InP NW ensemble contains a higher density of stacking faults, and therefore higher initial charge transfer rates across these heterointerfaces ought to be expected. We note that the observed PL emission decay is nonexponential (see inset Figure 3). This is expected as WZ segments have a distribution of lengths and electron–hole pairs are photo-generated at a range of distances away from interfaces with ZB segments. There will therefore be a distribution of times taken for electrons to diffuse within WZ segments to an interface at which electron transfer will occur, giving a time-dependent charge transfer rate. The relative independence of the observed PL decay rates on excitation fluence further suggests that even at the high injection densities employed here (10^{18} cm^{-3}) electron states available in ZB segments remain highly unsaturated, leaving the PL decay lifetimes unchanged over the excitation density used in this study. In summary, these spectroscopic investigations reveal that the PL emission decay is dominated by the transfer rate of charges across the type II interface, with 50 nm-InP NWs showing approximately twice the charge transfer rate of that observed for 160 nm-InP NWs, attributable to the higher density of such heterojunctions present in the 50 nm-InP NW ensemble.

We subsequently performed time-resolved PL spectral measurements at room temperature in order to assess how the presence of stacking faults in such nanowires affects the charge carrier cooling rates following nonresonant injection. Figure 4a shows representative transient PL spectra of 50 nm-InP NWs measured at different time delays at a charge injection density of $1.4 \times 10^{18} \text{ cm}^{-3}$. Charge carrier relaxation and cooling in inorganic semiconductors is known to evolve through a multitude of processes with a wide range of associated time scales.^{17–21} Nonresonant excitation will initially generate a nonequilibrium distribution of free charge carriers, whose rapid intraband relaxation will subsequently result in a thermalized Maxwell distribution characterized by a carrier temperature T_c .^{17,36} For the InP NWs, Figure 4a shows that the PL spectra center near the bandgap of the WZ phase within 300

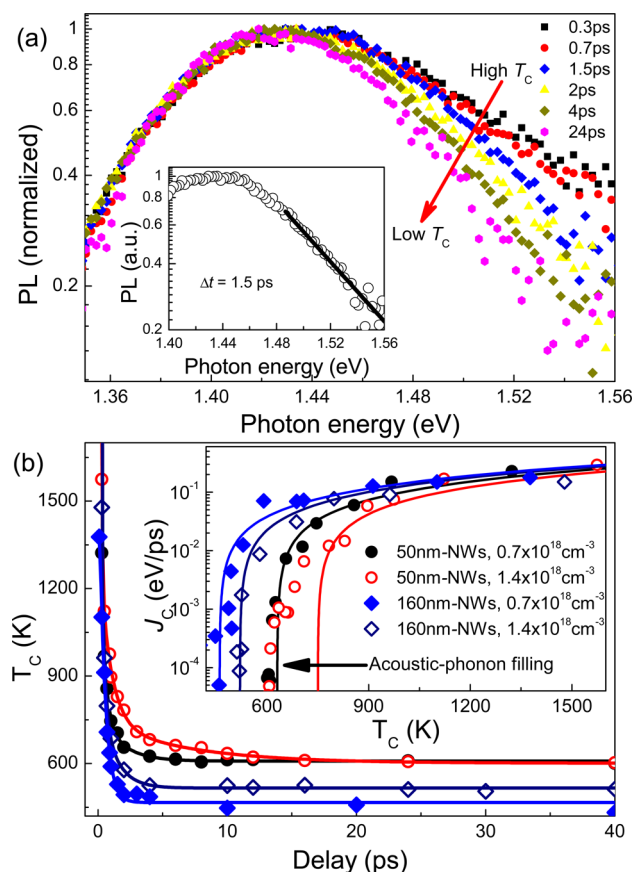


Figure 4. (a) Transient PL spectra of 50 nm-InP NWs measured at different time delays after photoexcitation generating a charge density of $1.4 \times 10^{18} \text{ cm}^{-3}$ at 300 K. The inset shows an example of an exponential fit (line) to the high-energy tail of the PL spectrum (dots) measured at time delay of 1.5 ps after the excitation. (b) The carrier temperature plotted as a function of time delay for 50 nm-InP NWs (circle) and 160 nm-InP NWs (diamond). The inset shows the energy loss rate of hot carriers (J_c) plotted as a function of carrier temperature T_c , extracted from the cooling curves in (b) for 50 nm-NWs (circle) and 160 nm-NWs (diamond) through numeric differentiation. The solid and empty symbols show the energy loss rate obtained at initial charge carrier densities of 0.7×10^{18} and $1.4 \times 10^{18} \text{ cm}^{-3}$, respectively. The solid lines are guides to the eye.

fs, which is matched by the rapid rise in transient PL intensity probed at the WZ band edge, as shown in Figure 3. These data demonstrate that, as expected, hot-carrier thermalization occurs on a time scale that is shorter than the temporal resolution of the measurement setup (≈ 200 fs). The subsequent cooling of this charge carrier distribution can be observed experimentally by analysis of the high-energy edge of the NW PL spectra, which is directly linked to the temperature of the hot-carrier distribution. The observed exponential dependence of this high-energy tail on photon energy (Figure 4a) confirms that carriers can be characterized by a Fermi–Dirac distribution with common temperature T_c , which can be well approximated by a Maxwell distribution.^{17,36,37} Hence we can extract T_c by fitting the high-energy edge of the spectra with $n \approx n_0 \exp(-\hbar\omega/k_b T_c)$, as illustrated in the inset of Figure 4a, where k_b is the Boltzmann’s constant, $\hbar\omega$ is the photon energy, and n is the carrier density.

Figure 4b plots the evolution of the carrier temperature extracted in this manner for both nanowires at different excitation densities. As reflected by the progressive increase of

the high-energy slope of the PL spectra with delay time, we find that the carrier temperature decreases rapidly following photoexcitation, which reflects the interaction dynamics of charge carriers with phonon modes, as discussed in more detail below. We find that by increasing the excitation density the carrier temperature at time delay >10 ps also increases, which suggests the buildup of a nonequilibrium phonon population, as generally observed in other bulk semiconductors^{18,24,25} at excitation densities in excess of 10^{18} cm^{-3} . Interestingly, we find that the T_c at longer time delays is always higher in 50 nm-InP NWs than in 160 nm-InP NWs, even at the lowest excitation density employed. In particular, we find that over the first 40 ps the carrier temperature only approaches the lattice temperature (300 K) for the 160 nm-InP NW ensemble at the lowest fluences but stays appreciably above it for the 50 nm-InP NWs and higher charge injection densities.

In order to illustrate better the mechanisms of charge-phonon interactions that underlie charge carrier cooling, we may convert the temporal evolution of T_c into a hot-carrier energy loss rate $J_c = (d/dt)(3k_b T_c/2)$. The inset of Figure 4b displays J_c as a function of carrier temperature, as extracted through numeric differentiation of the data shown in Figure 4b. We find that the initial energy loss rate is approximately 0.2 eV/ps for both nanowire ensembles and independent of the injection density. However, as the carrier temperature is reduced to ≈ 750 K, a sharp decrease in energy loss rates over several orders of magnitude is observed, which hampers further charge cooling. Such cooling behavior is similar to that observed in bulk semiconductors.^{17,18} Here, the initial rapid cooling is attributed to the strong carrier coupling to LO phonons which establishes a thermal equilibrium between the LO-phonon population and the electron–hole plasma. The initial cooling rate is therefore expected to be relatively independent of excitation density,¹⁸ as observed in the inset of Figure 4b. The subsequent, slower cooling of the plasma is determined by establishment of thermal equilibrium between LO phonons and acoustic phonons. The time scale for this process is determined by the anharmonic decay of zone-center LO phonons into two counterpropagating acoustic phonons, which occurs on the picosecond time scale in InP.^{38,39}

However, it has been shown that such phonon interconversion can be hampered by heating of the acoustic phonon bath, e.g., through use of high excitation fluences,⁴⁰ which results in an acoustic phonon temperature T_a that is significantly elevated with respect to the lattice temperature. The resulting slowdown of LO phonon decay from this “acoustic phonon bottleneck” will then affect further charge carrier cooling by rendering interactions between LO phonons and hot charge carriers less effective. In essence, the temperature at which the energy loss rate declines steeply is corresponding to the point at which the acoustic phonon bath temperature T_a becomes close to the carrier temperature T_c and the acoustic-phonon bottleneck is reached.^{17,18,20,24,25} Figure 4b shows that the acoustic-phonon bath temperature established within the first few picoseconds after excitation is hence considerably higher (≈ 600 K) for the 50 nm-InP NWs sample compared with that for the 160 nm-InP NWs (≈ 450 K) at the lowest injection density. Therefore, while the overall scenario is in accordance with an acoustic-phonon bottleneck limiting the charge carrier cooling in these nanowires, there is clear variation between the two nanowire ensembles in terms of the extent of such effects.

To display the general trends of charge carrier cooling with stacking fault density, Figure 5 shows collated data extracted

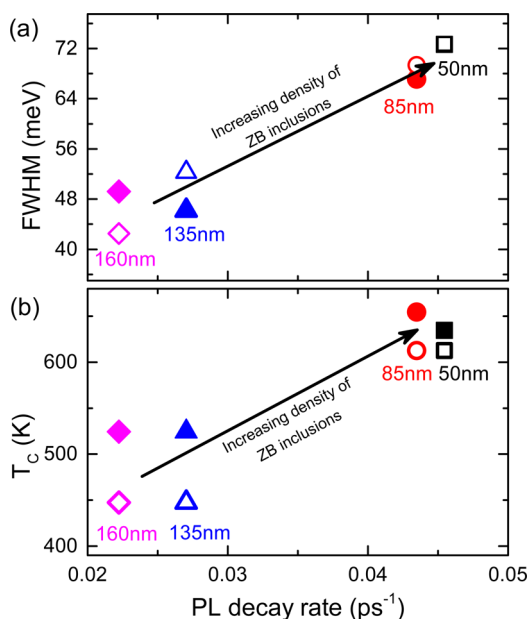


Figure 5. (a) Full width at half-maximum (fwhm) of time-integrated PL and (b) carrier temperature T_c at time delay $\Delta t = 10$ ps plotted as a function of PL decay rate (rate for the emission to decay to $1/e$ of its initial intensity) for InP NWs with average diameter (d) of 50 nm (black squares), 85 nm (red circles), 135 nm (blue triangles), and 160 nm (magenta diamonds) under low (empty) and high (solid) excitation fluences.

from all four nanowire samples. First, Figure 5a exhibits a clear correlation between the fwhm of the time-integrated PL spectra and the PL decay rate of the emission. These findings demonstrate that an increased density of WZ–ZB heterojunctions is reflected by a more inhomogeneous distribution of electronic states and leads to an increased rate of charge transfer across such interfaces that rapidly quenches the emission. As discussed above, the heterojunction defect density also appears to be correlated with nanowire diameter, showing two regimes of NWs with higher (50 and 85 nm) and lower (135 and 160 nm) stacking fault density. These data suggest that the choice of Au catalyst nanoparticle size not only affects the diameter of the resultant nanowire but also strongly influences stacking fault formation during the growth. Second, we may now use the knowledge gained on trends in stacking fault density to examine further links with charge carrier temperature. Figure 5b displays the carrier temperature at 10 ps after photoexcitation as a function of the PL decay rate, which reflects the spatial charge transfer rate across the type II heterojunction. These data show that the carrier temperature remains significantly higher in nanowire ensembles with higher stacking fault density. In addition, an increase of the excitation density leads to further increases in carrier temperature above the nominal lattice temperature. Since the carrier cooling on these time scales (>10 ps after excitation) is dominated by the acoustic phonon bottleneck, this plot further suggests that the acoustic phonon bath temperature becomes higher as the charge transfer rate is increased. Hence, we conclude that the carrier cooling in the nanowires containing type II heterojunctions is closely related to the dynamics of spatial charge transfer.

We may rule out the possibility of diameter-dependent nanowire cooling causing the observed trends. It has been shown that the decay of acoustic modes in semiconductor

nanostructures is mainly controlled by the heat-diffusion-limited interaction with the environment and therefore depends on the dimension and the surroundings of the nanostructure.^{20,41} Since the nanowires under investigation here predominantly lie flat on a quartz substrate, the heat dissipation is dominated by the radial diffusion from the nanowires to the substrate, which ought to be more effective for nanowires with smaller diameter (see Supporting Information). However, we predict that for our samples such cooling occurs over the nanosecond time scale (see Supporting Information), and we in fact observe the reverse effect of higher acoustic phonon bath temperatures for lower-diameter NW ensembles. Hence, we may eliminate the possibility of long-term sample heating effects causing the observed differences between nanowire ensembles.

Intraband energy relaxation in semiconductor nanostructures may occur through a variety of channels such as phonon emission, Auger relaxation, and nonadiabatic relaxation mediated by surface ligand vibrations.^{18,20,23,34,42} Our time-resolved PL and terahertz data (Figure 3) show no evidence for fluence-dependent dynamics or fast conductivity decay. Hence, we may rule out Auger relaxation and surface mediated relaxation as prominent channels for carrier cooling in these nanowires, at the excitation fluences employed. We propose instead a simple mechanism that links the observed differences in charge carrier cooling rates for the nanowire ensembles with the relative changes in the density of stacking faults they exhibit. Figure 6 schematically illustrates the charge carrier

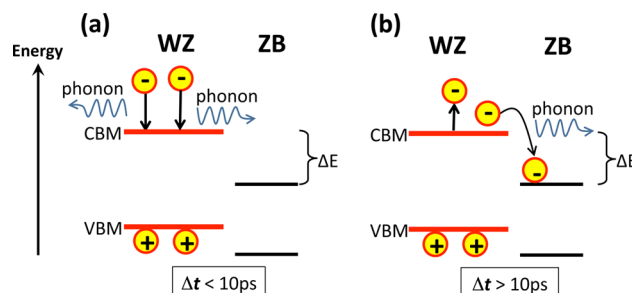


Figure 6. Schematic representation of the carrier cooling at semiconductor type II heterostructures: (a) Initial carrier cooling occurs via LO-phonon coupling at time delays $\Delta t < 10$ ps after photoexcitation. (b) At $\Delta t > 10$ ps after photoexcitation, charge transfer across the WZ–ZB type II interface releases an excess energy comparable to the energetic offset across the heterojunction (ΔE), which results in further phonon emission.

dynamics following injection into the WZ segments of the nanowires. Charge carrier cooling will happen through the release of phonons, but over the time scale of the first tens of picoseconds, spatial charge transfer across the WZ–ZB type II heterojunction will occur concurrently. The intraband relaxation in the ZB phase will lead to an additional release of excess energy following the spatial charge separation, which is transferred to the lattice via further phonon emission (Figure 6a,b). As a result, the buildup of a nonequilibrium phonon population is augmented significantly over the time scale on which such charge transfer processes occur (few tens of picoseconds). Such carrier relaxation from the conduction band of WZ to the energetically lower-lying electronic states of ZB is similar to inter-subband transitions in quantum wells, where sizable excess energy is released to the lattice.^{43,44} For the nanowire ensembles under investigation here, we observe a

clear correlation between the density of stacking faults present and the carrier temperature T_c attained by the acoustic phonon bath within the first few picoseconds after excitation (see Figure 5). Since the direct band-to-band PL recombination from the WZ phase competes with the spatial charge transfer across the WZ–ZB type II heterojunctions, the higher charge transfer rate across the type II heterojunction will lead to a higher energy transfer rate to the acoustic phonon bath. In addition, such spatial separation of electrons and holes has been shown to enhance the coupling of charge carriers to LO phonons.^{23,42} Hence, nanowires with higher charge-transfer rates will exhibit faster cooling of charge carriers via more efficient emission of LO phonons. The subsequent anharmonic decay of these LO phonons leads to a buildup of an acoustic phonon population that only slowly decays over times scales of hundreds of picoseconds. In turn, this increase in the population of nonequilibrium phonons will significantly decrease carrier cooling rates.^{18,24,25} In accordance with our observations, nanowires exhibiting higher densities of such stacking defects will therefore more effectively sustain charge carriers at an elevated temperature.

In conclusion, we demonstrate for the first time that type II heterointerfaces in semiconductor nanowires can allow for a hot charge carrier distribution to be maintained over an extended time period. One beneficial aspect of such slowed carrier cooling is that the presence of stacking faults may not be detrimental to the efficiency of solar cells based on the nanowires. Nonresonant photoexcitation in general results in substantial irreversible solar energy loss to the lattice via phonon emission within first few picoseconds. Theoretical calculations suggest that a reduction of the hot-carrier cooling rate can significantly improve the highest achievable efficiency of a solar cell.⁴⁵ In particular, we have recently shown that the radial transfer of charge carriers from inorganic semiconductor nanowires of similar diameter to a surrounding polymer matrix can be completed within a few tens of picoseconds.²⁸ Here we find that over such time scales excess energy is maintained in the hot-carrier distribution, which may hence be utilized in the charge transfer into a surrounding organic matrix. Our results thus imply that hot-carrier harvesting is potentially feasible in hybrid photovoltaic materials containing nanowires with stacking faults.

■ ASSOCIATED CONTENT

Supporting Information

Experimental details. This material is available free of charge via the Internet at <http://pubs.acs.org>.

■ AUTHOR INFORMATION

Corresponding Author

*E-mail: l.herz@physics.ox.ac.uk (L.M.H.).

Notes

The authors declare no competing financial interest.

■ ACKNOWLEDGMENTS

The authors acknowledge financial support from the Engineering and Physical Sciences Research Council (UK), the Australian Research Council, and the Australian National Fabrication Facility.

■ REFERENCES

- (1) Gur, I.; Fromer, N. A.; Geier, M. L.; Alivisatos, A. P. *Science* **2005**, *310*, 462–465.
- (2) Puthussery, J. *ACS Nano* **2008**, *2*, 357–367.
- (3) Wang, J. F.; Gudiksen, M. S.; Duan, X. F.; Cui, Y.; Lieber, C. M. *Science* **2001**, *293*, 1455–1457.
- (4) Duan, X. F.; Huang, Y.; Cui, Y.; Wang, J. F.; Lieber, C. M. *Nature* **2001**, *409*, 66–69.
- (5) Novotny, C. J.; Yu, E. T.; Yu, P. K. L. *Nano Lett.* **2008**, *8*, 775–779.
- (6) Wallentin, J.; Anttu, N.; Asoli, D.; Huffman, M.; Aberg, I.; Magnusson, M. H.; Siefert, G.; Fuss-kailuweit, P.; Dimroth, F.; Witzigmann, B.; Xu, H. Q.; Samuelson, L.; Deppert, K.; Borgström, M. T. *Science* **2013**, *339*, 1057–1060.
- (7) Titova, L. V.; Hoang, T. B.; Yarrison-Rice, J. M.; Jackson, H. E.; Kim, Y.; Joyce, H. J.; Gao, Q.; Tan, H. H.; Jagadish, C.; Zhang, X.; Zou, J.; Smith, L. M. *Nano Lett.* **2007**, *7*, 3383–3387.
- (8) Duan, X. F.; Lieber, C. M. *Adv. Mater.* **2000**, *12*, 298–302.
- (9) Wallentin, J.; Mergenthaler, K.; Ek, M.; Wallenberg, L. R.; Samuelson, L.; Deppert, K.; Pistol, M. E.; Borgström, M. T. *Nano Lett.* **2011**, *11*, 2286–2290.
- (10) Mattila, M.; Hakkarainen, T.; Mulot, M.; Lipsanen, H. *Nanotechnology* **2006**, *17*, 1580–1583.
- (11) Ikejiri, K.; Kitauchi, Y.; Tomioka, K.; Motohisa, J.; Fukui, T. *Nano Lett.* **2011**, *11*, 4314–4318.
- (12) Wang, F.; Reece, P. J.; Paiman, S.; Gao, Q.; Tan, H. H.; Jagadish, C. *Nano Lett.* **2011**, *11*, 4149–4153.
- (13) Pemasiri, K.; Montazeri, M.; Gass, R.; Smith, L. M.; Jackson, H. E.; Yarrison-Rice, J.; Paiman, S.; Gao, Q.; Tan, H. H.; Jagadish, C.; Zhang, X.; Zou, J. *Nano Lett.* **2009**, *9*, 648–654.
- (14) Bao, J.; Bell, D. C.; Capasso, F.; Wagner, J. B.; Mårtensson, T.; Trägårdh, J.; Samuelson, L. *Nano Lett.* **2008**, *8*, 836–841.
- (15) Zhang, L.; Luo, J.; Zunger, A.; Akopian, N.; Zwiller, V.; Harmand, J. *Nano Lett.* **2010**, *10*, 4055–4060.
- (16) Akopian, N.; Patriarche, G.; Liu, L.; Harmand, J. C.; Zwiller, V. *Nano Lett.* **2010**, *10*, 1198–1201.
- (17) Yoon, H. W.; Wake, D. R.; Wolfe, J. P. *Phys. Rev. B* **1996**, *54*, 2763–2774.
- (18) Klimov, V.; Bolivar, P. H.; Kurz, H. *Phys. Rev. B* **1995**, *52*, 4728–4731.
- (19) Pop, E. *Nano Res.* **2010**, *3*, 147–169.
- (20) Achermann, M.; Bartko, A. P.; Hollingsworth, J. A.; Klimov, V. I. *Nat. Phys.* **2006**, *2*, 557–561.
- (21) Tisdale, W. A.; Williams, K. J.; Timp, B. A.; Norris, D. J.; Aydil, E. S.; Zhu, X. Y. *Science* **2010**, *328*, 1543–1547.
- (22) Bindl, D. J.; Safran, N. S.; Arnold, M. S.; Parkinson, B. *Science* **2010**, *330*, 63–66.
- (23) Kambhampati, P. *Acc. Chem. Res.* **2011**, *44*, 1–13.
- (24) Lugli, P.; Goodnick, S. M. *Phys. Rev. Lett.* **1987**, *59*, 716–719.
- (25) Kash, J. A.; Tsang, J. C.; Hvam, J. M. *Phys. Rev. Lett.* **1985**, *54*, 2151–2154.
- (26) Murayama, M.; Nakayama, T. *Phys. Rev. B* **1994**, *49*, 4710–4724.
- (27) Yong, C. K.; Joyce, H. J.; Lloyd-Hughes, J.; Gao, Q.; Tan, H. H.; Jagadish, C.; Johnston, M. B.; Herz, L. M. *Small* **2012**, *8*, 1725–1731.
- (28) Yong, C. K.; Noori, K.; Gao, Q.; Joyce, H. J.; Tan, H. H.; Jagadish, C.; Giustino, F.; Johnston, M. B.; Herz, L. M. *Nano Lett.* **2012**, *12*, 6293–6301.
- (29) Parkinson, P.; Joyce, H. J.; Gao, Q.; Tan, H. H.; Zhang, X.; Zou, J.; Jagadish, C.; Herz, L. M.; Johnston, M. B. *Nano Lett.* **2009**, *9*, 3349–3353.
- (30) Joyce, H. J.; Wong-Leung, J.; Yong, C. K.; Docherty, C. J.; Pauman, S.; Gao, Q.; Tan, H. H.; Jagadish, C.; Lloyd-Hughes, J.; Herz, L. M.; Johnston, M. B. *Nano Lett.* **2012**, *12*, 5325–5330.
- (31) Chang, M. H.; Hoeben, F. J. M.; Jonkheijm, P.; Schenning, A. P. H. J.; Meijer, E. W.; Silva, C.; Herz, L. M. *Chem. Phys. Lett.* **2006**, *418*, 196–201.
- (32) Yu, P. Y.; Cardona, M. *Fundamentals of Semiconductors*; Springer-Verlag: Heidelberg, 1996.

- (33) Joyce, H. J.; Docherty, C. J.; Gao, Q.; Tan, H. H.; Jagadish, C.; Lloyd-Hughes, J.; Herz, L. M.; Johnston, M. B. *Nanotechnology* **2013**, *24*, 214006.
- (34) Cooney, R. R.; Sewall, S. L.; Anderson, K. E. H.; Dias, E. A.; Kambhampati, P. *Phys. Rev. Lett.* **2007**, *98*, 177403–177406.
- (35) Klimov, V. I.; Mikhailovsky, A. A.; McBranch, D. W.; Leatherdale, C. A.; Bawendi, M. G. *Science* **2000**, *287*, 1011–1013.
- (36) Elsaesser, T.; Shah, J.; Rota, L.; Lugli, P. *Phys. Rev. Lett.* **1991**, *66*, 1757–1760.
- (37) Snoke, D. W.; Ruhle, W. W.; Lu, Y. C.; Bauser, E. *Phys. Rev. Lett.* **1992**, *68*, 990–993.
- (38) Grann, E. D.; Tsen, K. T.; Ferry, D. K. *Phys. Rev. B* **1996**, *53*, 9847–9851.
- (39) Shah, J. *Ultrafast Spectroscopy of Semiconductors and Semiconductor Nanostructures*, 1st ed.; Springer: Berlin, 1996.
- (40) Ryan, J. F.; Taylor, R. A.; Turberfield, A. J.; Maciel, A.; Worlock, J. M.; Gossard, A. C.; Wiegmann, W. *Phys. Rev. Lett.* **1984**, *53*, 1841–1844.
- (41) Ge, Z.; Cahill, D. G.; Braun, P. V. *J. Phys. Chem. B* **2004**, *108*, 18870–18875.
- (42) Banerjee, S.; Maity, S.; Datta, A. *J. Phys. Chem. C* **2011**, *115*, 22804–22809.
- (43) Seilmeier, A.; Hubner, H. J.; Abstreiter, G.; Weimann, G.; Schlapp, W. *Phys. Rev. Lett.* **1987**, *59*, 1345–1348.
- (44) Oberli, D. Y.; Wake, D. R.; Klein, M. V.; Klem, J.; Henderson, T.; Morkoç, H. *Phys. Rev. Lett.* **1987**, *59*, 696–699.
- (45) Ross, R. T.; Nozik, A. J. *J. Appl. Phys.* **1982**, *53*, 3813–3818.